Journal of Materiomics 11 (2025) 100993

Contents lists available at ScienceDirect

Journal of Materiomics

journal homepage: www.journals.elsevier.com/journal-of-materiomics/

Research paper

Multifunctional energy storage and photoluminescence of Er-modified KNN-based transparent ferroelectric ceramics

Zhichao Gong [a], Haojie Yue [a], Kailing Fang [a], Kun Guo [a,*], Kang Li [a], Chong Guo [a], Huacheng Zhang [a], Ziliang Deng [a], Zhiyong Liu [a], Bing Xie [a], Pu Mao [a], Jinshan Lu [a], Shifeng Guo [b], Kui Yao [c], Francis Eng Hock Tay [d]

[a] School of Power and Energy, Nanchang Hangkong University, Nanchang, 330063, China
[b] Shenzhen Key Laboratory of Smart Sensing and Intelligent Systems, Shenzhen Institute of Advanced Technology, Chinese Academy of Sciences, 1068 Xueyuan Avenue, Shenzhen University Town, Shenzhen, 518055, Guangdong, China
[c] Institute of Materials Research and Engineering(IMRE), A*STAR (Agency for Science, Technology and Research), 2 Fusionopolis Way, Innovis, 138634, Singapore
[d] Department of Mechanical Engineering, National University of Singapore, 9 Engineering Drive 1, 117575, Singapore

ARTICLE INFO

Article history:
Received 24 September 2024
Received in revised form
20 November 2024
Accepted 24 November 2024
Available online 15 December 2024

Keywords:
KNN
Upconversion photoluminescence
Multifunctional ceramics
First-principles calculation

ABSTRACT

Against the backdrop of increasing miniaturization and integration of electronic components, the demand for materials with multifunctionality has increased significantly. Among these, transparent fluorescent ferroelectric ceramics exhibiting ferroelectricity, optical transparency, and photoluminescence (PL) have garnered significant attention. However, an interdependent relationship exists in a ferroelectric material among polarization, transparency, and photoluminescence, which presents a challenge for optimizing the coupling of optoelectronic properties. In this work, the doping concentration of Er^{3+} in $0.825(K_{0.5}Na_{0.5})NbO_3$-$0.175Sr(Sc_{0.5}Nb_{0.5})O_3$: x%Er (x = 0–0.15) system was modulated by first-principle calculations through compositional design and performance-influencing-factor-analysis strategies. The experimental results showed that grain size of the ceramic was reduced to 28 μm at x = 0.05, concentration of vacancy defects in the lattice was low, and band gap value was increased to 3.105 eV. The multifunctional ceramic, while maintaining an excellent recoverable energy storage density (W_{rec} = 2.03 J/cm^3) and energy storage efficiency (η = 75.67%), demonstrated a 56% (1100 nm) good near-infrared transmittance and upconversion photoluminescence properties at 527, 549 nm, and 667 nm exhibiting weak green, strong green, and weak red light, respectively. This study provides a theoretical foundation and new approach for realizing the multifunctionality of photoelectric couple by introducing rare earth elements as luminescent centers into ferroelectric ceramics.

1. Introduction

As electronic components move towards miniaturization and integration, single-function materials can no longer meet the increasingly complex and varied needs of electronic devices [1–6]. The development of integrated multifunctional materials has become a hot research topic in the field of electronic components [7–13]. Ferroelectric ceramics are regarded as an ideal substrate for realizing multifunctional materials due to their ferroelectric properties and high-temperature stability [14–17]. The introduction of Sm^{3+} into BNT-BT ceramics enables synergistic enhancement of electrical and luminescent properties, providing new possibilities for the development of optoelectronic integration and coupling devices [18]. PNN-PZT ceramics exhibit piezoelectric effects and varistor properties, enabling kinetic responses to specific critical application scenarios [19]. The diverse physical environments triggered by different doping sites of Ce in BT-based ceramics, the feasibility of multifunctional BT-based ferroelectric ceramics with excellent electrothermal and electrostrictive effects is verified [20,21]. Rare earth elements are often used as active ions in luminescent materials due to their unique 4f inner layer structure [22–25]. By introducing rare earth elements into ferroelectric ceramics as light-emitting centers, the versatility of optoelectronic

* Corresponding author.
E-mail address: guokun@nchu.edu.cn (K. Guo).
Peer review under responsibility of The Chinese Ceramic Society.

https://doi.org/10.1016/j.jmat.2024.100993

coupling can be realized, which provides strong support for the development of new functional materials [26–29]. To integrate the optical properties into the ferroelectric system, low phonon energy host materials with nonradiative relaxation properties were selected, which can effectively improve the fluorescence lifetime and upconversion photoluminescence (UCPL) efficiency of RE intermediate energy levels [30,31]. KNN-based ferroelectric ceramics exhibit excellent dielectric, ferroelectric, and optical properties and are considered as one of the most promising lead-free multifunctional ferroelectric ceramics [32–36]. Their low phonon energy levels also make them suitable PL substrates. Therefore, KNN-based ceramics have been noticed and studied in the field of multifunctional transparent ferroelectric materials [37–39].

Sm^{3+}-doped $(K_{0.5}Na_{0.5})NbO_3$ transparent ceramics have exhibited reversible photochromic (PC) behavior and the related modulation of transmittance and luminous intensity [40]. Ho^{3+}-doped $(K_{0.5}Na_{0.5})NbO_3$–$SrTiO_3$ transparent ceramics exhibit high transmittance in the near-infrared (NIR) region (~70%) and possess a stable emissive color at low temperature [41]. Among rare earth ions, erbium (Er) is one of the most commonly used upconversion ions. Its energy level structure includes a $^4I_{15/2} \rightarrow {}^4I_{11/2}$ transition, a process highly responsive to low-energy photon excitation [42]. Er-doped $(K_{0.5}Na_{0.5})NbO_3$-(Ba, Sr)TiO_3 ceramics demonstrate a high degree of reversible modulation in transparency, photoluminescence intensity, and conductivity. These properties endow the ceramic material with an exceptional ability to store and modulate optoelectronic information [43]. KNNLB-Er ceramics demonstrate 50% transmittance in the visible range with notable modulation contrast, where ΔAbs reaches 16.2%, and Δ*R* is 34% [44]. However, there is a scarcity of report on ferroelectric materials that possess photoluminescence (PL) performance while maintaining both significant energy storage properties and high transmittance, both experimentally and mechanistically. Therefore, there is an urgently needed to develop a transparent ferroelectric ceramic material that enables the effective coexistence of transmittance, luminescence, and electrical properties.

In this investigation, by adopting a composition-performance influencing factor strategy, different concentrations of Er^{3+} were doped into the KNN-SSN system through density functional theory (DFT) calculations, and the changes in electronic structure and related properties were assessed semi-quantitatively. The 0.825KNN-0.175SSN: *x*%Er multifunctional ceramics exhibit not only excellent energy storage characteristics and high transmittance but also significant photoluminescence effects. As illustrated in Fig. 1, optimized doping of Er^{3+} has reduced the grain size of the material, significantly enhancing its energy storage performance. The combined effects of lattice distortion, changes in vacancy concentration, and an increase in bandgap energy have collectively contributed to the remarkable transparency and upconversion photoluminescence (UCPL) behavior as observed. Our systematic analysis of the crystal structure, ferroelectric properties, and optical characteristics of the ceramics, the underlying mechanisms offers both a theoretical foundation and practical guidance for developing high-performance multifunctional optoelectronic devices.

2. Experimental section

Ceramic samples were prepared by stoichiometric ratio $0.825(K_{0.5}Na_{0.5})NbO_3$-$0.175Sr(Sc_{0.5}Nb_{0.5})O_3$: *x*%Er (*x* = 0, 0.05, 0.10, 0.15) from starting chemical reagents K_2CO_3 (99.0%), Na_2CO_3 (99.8%), Nb_2O_5 (99.5%), $SrCO_3$ (99.0%), Sc_2O_3 (99.9%), Er_2O_3 (99.9%). After the raw materials were weighed, the ball mill for the raw mixture was performed with anhydrous ethanol for 12 h, and then the mixed slurry was dried at 80 °C until the anhydrous ethanol was completely volatilized. The dried mixture was calcined in a crucible at 950 °C for 5 h, and then the calcined powder was ball-milled again for 12 h. After drying, the powder was mixed with 5% (mass fraction) PVA solution and ground. Then, disk-like samples with a diameter of 12 mm and a thickness of 0.3–0.5 mm were obtained by isostatic pressing at 250 MPa. Finally, the samples were sintered at 1200–1300 °C for 2 h, and then polished to a thickness of 0.3 mm for transmittance test, and polished to a thickness of 0.15 mm for ferroelectric performance measurement.

The phase structure of the samples was characterized by X-ray diffraction (XRD, D8 Advance A25, Bruker, Germany). The surface microstructure and element localization of the samples were detected by field emission scanning electron microscopy (FE-SEM, Nova Nano SEM450, FEI, Czech). The distribution of the corresponding particle size was estimated by FESEM micrograph measurement. The transmittance of the sample was measured using an ultraviolet–visible spectrophotometer (UV-3600, Shimadzu Co, Japan). Upconversion photoluminescence spectra were measured under 980 nm laser excitation (FLS1000, Edinburgh). The dielectric response spectra at different frequencies and temperature ranges were measured using a precision impedance analyzer (LCR meter, TH2382, China). The polarization electric field (*P*–*E*) hysteresis loop was measured at 100 Hz using a ferroelectric test system (PolyK Technologies, USA). The AC impedance spectra were measured by an electrochemical workstation (CHI700e, CH Instruments Ins, China) from 460 °C to 640 °C. X-ray photoelectron spectroscopy (XPS, Axis Ultra DLD, United Kingdom).

First-principles calculations were performed using Materials Studio software based on density functional theory (DFT) and the supercell method in conjunction with the virtual crystal approximation (VCA). To address electron-electron interactions, the Perdew-Burke-Ernzerhof (PBE) functional within the generalized gradient approximation (GGA) was utilized [45].

The supercell calculation of KNN-SSN: *x*%Er systems with different components was carried out, and the atomic-scale theoretical model of KNN-based systems was constructed. Specifically, a 2 × 3 × 3 orthogonal KNN supercell was established by the particular quasi-random structure (SQS) method, containing 150 atoms [46]. The calculated formation energy information at different positions in the Er-substituted KNN lattice (see Fig. 1) shows that both E_f (Er→Nb) and E_f (Er→O) are positive, while E_f (Er→K) and E_f (Er→Na) are negative, and E_f (Er→Na) is slightly lower than E_f (Er→K). From the thermodynamic point of view, it is shown that Er mainly replaces Na at the A-site. This confirms that Er is thermodynamically favorable for the A-site doping of the KNN-SSN system, and Er doping can be achieved by introducing Er_2O_3 into the KNN-SSN system.

By varying the A-site K, Na, and Sr atoms and the B-site Nb, Sc, and O atoms, different levels of Er^{3+} doping were introduced into the KNN-SSN system using the VCA method. The wave functions were expanded using a plane wave basis set with a cut-off energy of 620 eV, while Brillouin zone integration was performed with a 7 × 7 × 7 Monkhorst-Pack k-point grid. The energy convergence criterion was set to less than 1×10^{-6} eV/atom, and the force convergence criterion was set to less than 0.01 eV/Å. The Doml3 module was employed for crystal orbital overlap population (COOP) analysis to effectively elucidate the orbital overlap effects.

3. Results and discussion

The X-ray diffraction (XRD) patterns of 0.825KNN-0.175SSN: *x*% Er (*x* = 0, 0.05, 0.10, 0.15) ceramics with different contents at room temperature as well as localized magnification in the range of 45°–46° are shown in Fig. 2a. The results show that all samples have a pure chalcogenide single-phase structure without impurity

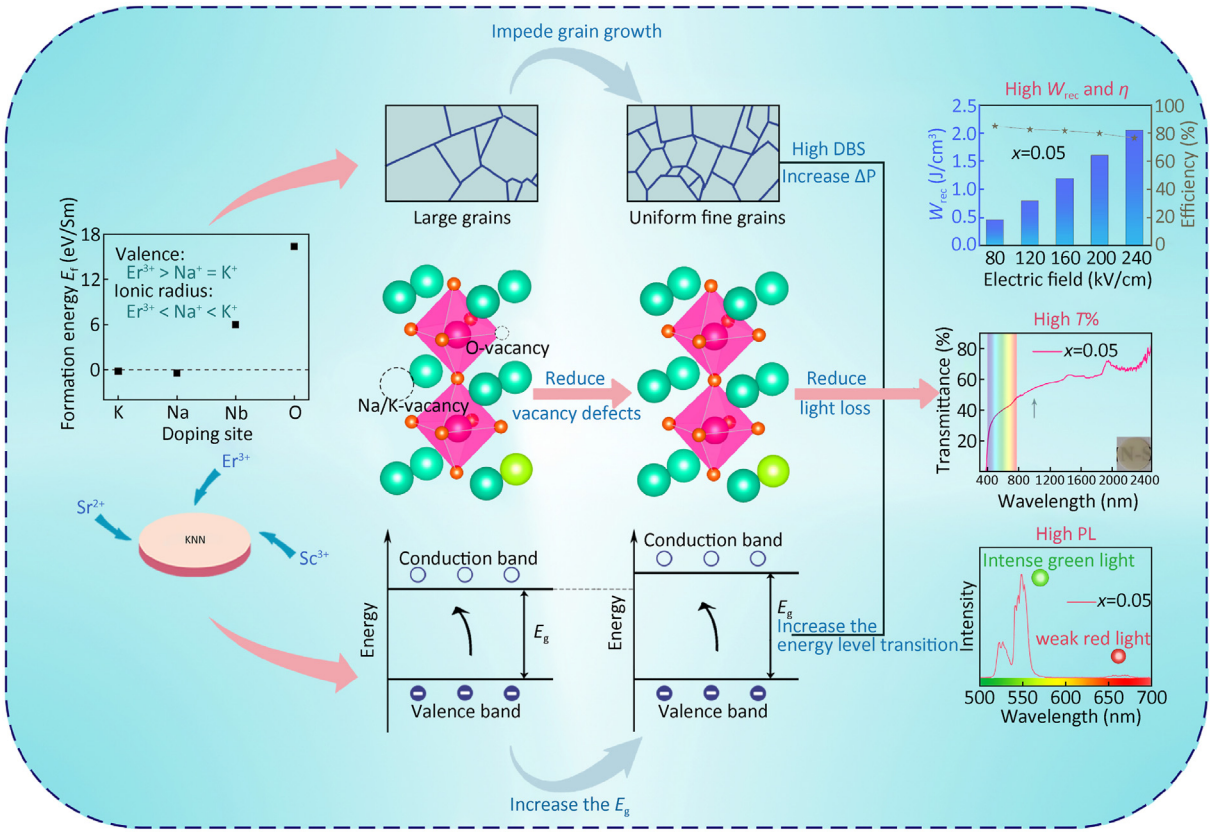

Fig. 1. Schematic diagram of the strategy for tuning energy storage performance, transmittance, and photoluminescence behavior of 0.825KNN-0.175SSN ceramics by doping with Er^{3+}.

secondary phases, indicating that Er^{3+}, Sr^{2+}, and Sc^{3+} have diffused into the KNN lattice to form a new solid solution. The doping element Er^{3+} ions, which have a radius (1.23 Å, CN = 12) close to that of the host K^+ (1.64 Å, CN = 12), Na^+ (1.39 Å, CN = 12), and Sr^{2+} ions (1.44 Å, CN = 12), will preferentially occupy the A-sites of the ABO_3 chalcogenide structure, which leads to lattice contraction. The localized magnified image shows that the diffraction peak position shifts to a higher angle with increasing Er content, further confirming this substitution phenomenon. A single peak of (200) is present in all samples in the 45°–46° angle range for a pseudo-cubic phase structure with high symmetry. Ceramics with pseudo-cubic crystal structures usually have high optical transparency due to the small light scattering at the grain boundaries of isotropic lattice structures [47,48].

To accurately quantify the changes in the phase structure and lattice parameters of the 0.825KNN-0.175SSN: *x*%Er ceramics, a tetragonal-phase (*P*4*mm*) based Rietveld refinement was performed using GSAS software [49,50]. Additional details of the relevant Rietveld refinement structural parameters and tetragonality (*c*/*a*) are shown in Table S1 and Fig. 2b. Reliability coefficients (R_{wp} and R_p) are below 10%, which ensures the confidence of the final refined fitting results. The lattice parameters *a*, *b*, and *c* vary significantly with increasing Er content, leading to different degrees of lattice distortion. The *c*/*a* ratio is commonly used to characterize the degree of lattice distortion in tetragonal phases, and the more the value deviates from 1, the lower the structural symmetry [51]. Fig. 2c–d illustrate the Rietveld refinement results for the $x = 0$ and $x = 0.05$ components, respectively. The results for the remaining components are shown in Fig. S1. Compared to the 0.825KNN-0.175SSN (*c*/*a* = 0.99997), the *c*/*a* ratio increases to 1.00001 at $x = 0.05$, indicating enhanced symmetry of the structure after doping. Fig. 2e demonstrates the change in atomic displacement in the oxygen octahedron before and after doping, where the B-site Nb ion moves along the [001] direction, resulting in an increase in the Nb–O_{a2} bond length and a decrease in the Nb–O_{a1} bond length. This change results in an increase in the O–Nb–O bond angles in the octahedra and an improvement in the lattice symmetry.

Microstructural scanning of the thermally corroded surface of the ceramic samples after polishing was carried out using field emission scanning electron microscopy (FE-SEM) to investigate the effect of Er doping on the grain size of 0.825KNN-0.175SSN ceramic, and the relevant results are shown in Fig. 3a–d. The results showed that all ceramic samples exhibited a dense microstructure without obvious pores. With the increase of Er content, the average grain size of the ceramic samples showed a tendency to decrease and then increase, as shown in Fig. 3e. Especially at $x = 0.05$, the ceramic grains were fine and uniform, with a high density of grain boundaries, which helped to obtain high DBS and excellent transparency [52,53]. This indicates that a moderate amount of Er can effectively inhibit the grain growth of 0.825KNN-0.175SSN ceramics. This may be related to the doping of Er^{3+} as a high valence donor, when Er^{3+} replace the A-site in the KNN lattice, additional cationic vacancies (*e.g.*, V'_K or V'_{Na}) are generated to maintain the space charge balance due to the difference in valence states [54]. This leads to a decrease in the lattice diffusion coefficient and a weakening of mass transfer, thus inhibiting grain growth [38,55]. In addition, reducing the grain size helps to enhance the coupling effect between grains and grain boundaries, which in turn hinders the domain flip, and is conducive to lowering the residual polarization strength and improving the

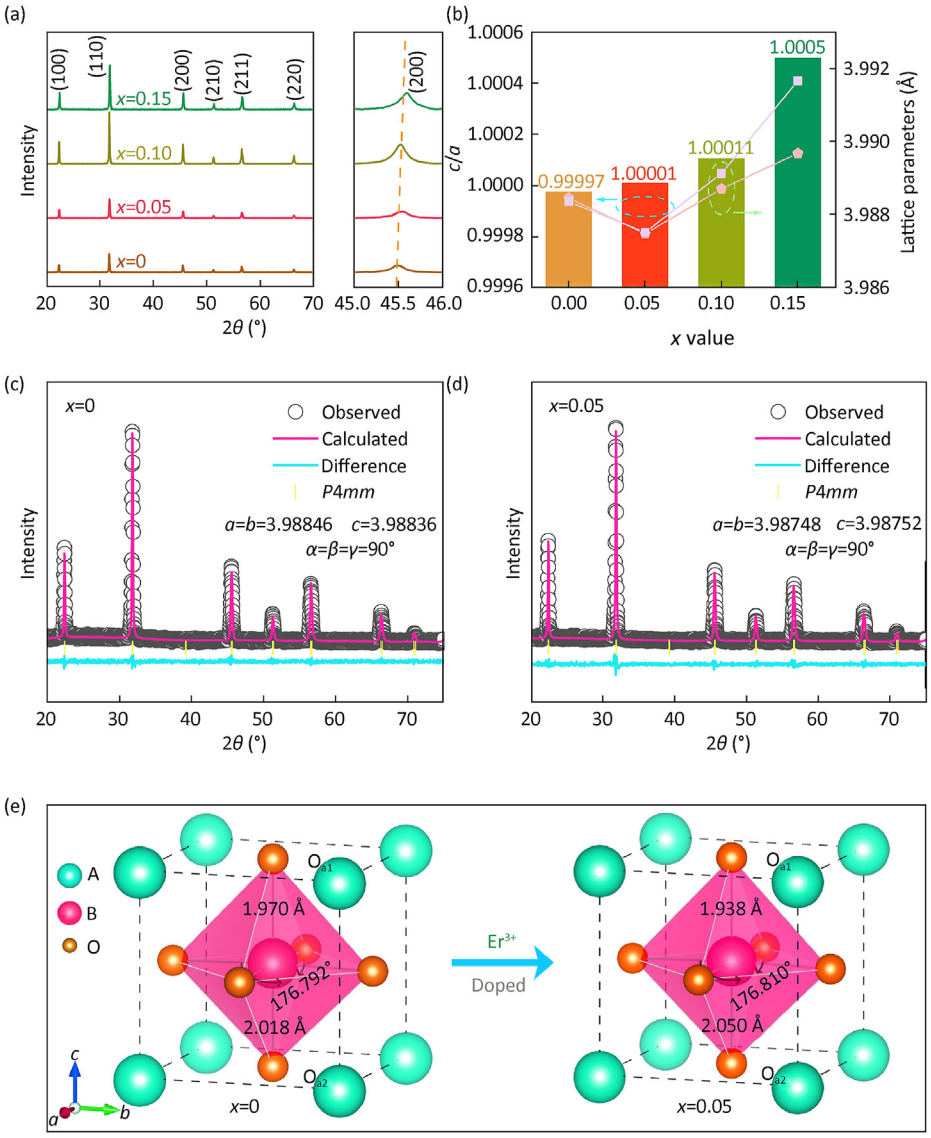

Fig. 2. 0.825KNN-0.175SSN: *x*%Er ceramics in the 2θ range of (a) XRD spectra at 20°–70° and 45°–46°; (b) Values of the lattice parameters *a*, *b*, *c* and the *c*/*a* ratio; Rietveld refinement results for (c) $x = 0$ and (d) $x = 0.05$ samples; (e) Schematic representation of the protocell structure of doped and undoped ceramics.

energy storage performance [56,57]. EDS spectroscopic analyses confirmed the presence of the elements K, Na, Sr, Sc, Nb, O, and Er in the samples, as shown in Fig. 3f.

The measure of transparency is the percentage of the remaining light energy *I* to the total energy *T* after the light with an energy of I_0 passes through the material [57–60]. Formula (1) is as follows:

$$T = \frac{I}{I_0} = (1 - R_2)\exp[-(\gamma + \alpha) \cdot t] \quad (1)$$

where *T* is the transmittance, R_2 is the reflection loss of the sample on two surfaces, γ is the total scattering coefficient, α is the absorption coefficient, and *t* is the thickness [61]. For polycrystalline ceramics, light scattering caused by a large number of grain boundaries and pores inside is the main factor affecting transparency [62]. The transmission spectra and photos of 0.825KNN-0.175SSN: *x*%Er ceramics are shown in Fig. 4a. Through the ceramic sheet, the letters on the paper can still be distinguished. It can be seen from Fig. 4a that the transmittance of the $x = 0.05$ ceramic sample in the visible light (780 nm) and near-infrared region (1100 nm) is 48% and 56%, respectively. This may be due to the decrease in light scattering and the increase of light transmittance caused by the high symmetry of the pseudo-cubic phase lattice ($c/a = 1.00001$) and the small grain size. According to the Tauc equation, the optical band gap value (E_g) can be estimated from the absorption spectrum:

$$(\alpha h\nu)^2 = A(h\nu - E_g) \quad (2)$$

where ν is the photon frequency, *h* is Planck's constant ($h = 4.13571015$ eV), and *A* is a constant and α is the $-\lg(T)$ value [61]. Based on the obtained values of $(\alpha h\nu)^2$ *versus* $h\nu$, the band gap plots of different components are plotted as shown in Fig. 4b. The intercept of the curve with the *x*-axis is the band gap value. The sample with $x = 0.05$ has the largest E_g value (3.04 eV). Higher E_g value helps to reduce the energy consumption of electron leaps and thus increases the transmittance following the law of transmittance.

The upconversion spectra and luminescence mechanism of 0.825KNN-0.175SSN: *x*%Er ceramics are presented in Fig. 4c–d.

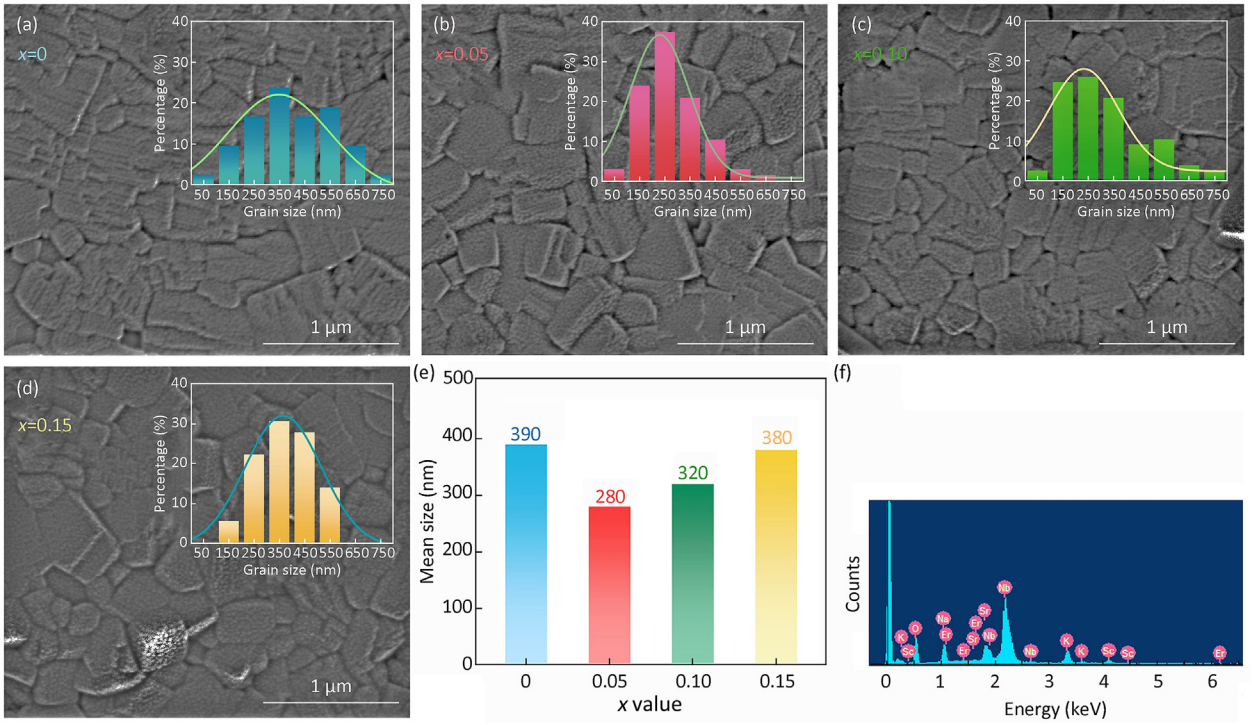

Fig. 3. SEM micrographs of the polished and thermally corroded surfaces of 0.825KNN-0.175SSN: *x*%Er ceramics with insets showing histograms of the grain size distributions: (a) $x = 0$; (b) $x = 0.05$; (c) $x = 0.10$; (d) $x = 0.15$; (e) Average grain sizes of the component ceramics; (f) Elemental EDS spectra of the $x = 0.05$ ceramic samples.

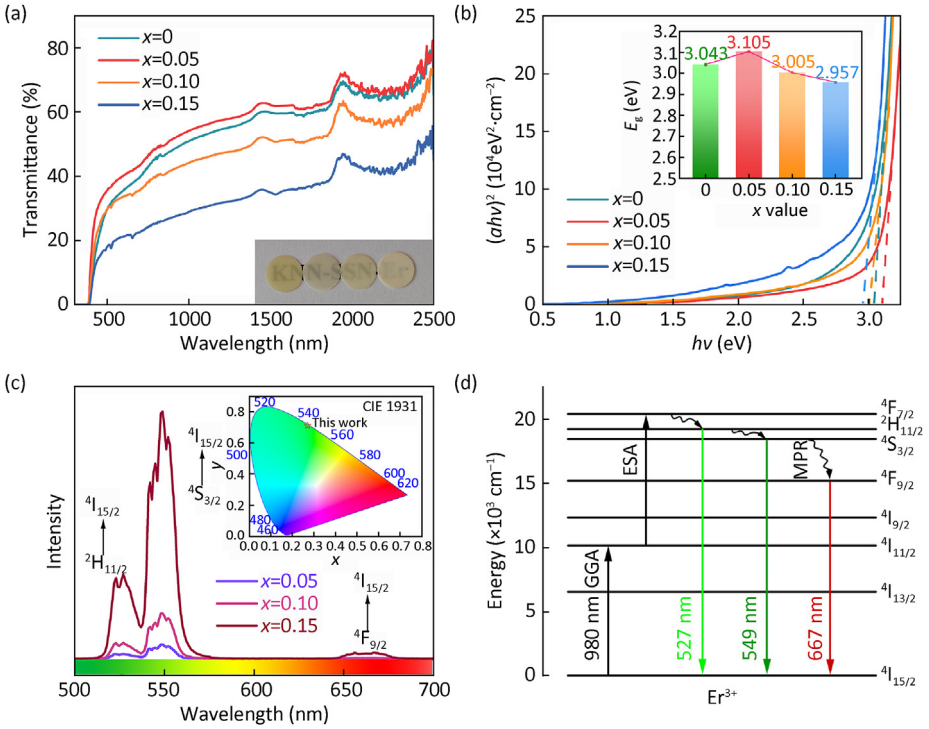

Fig. 4. (a) Optical transmission spectra and photographs of 0.825KNN-0.175SSN: *x*%Er ceramic samples; (b) Plot of $(\alpha h\nu)^2$ *vs.* $h\nu$, with the inset showing the bandgap columnar distribution of each component; (c) UCPL spectra of 0.825KNN-0.175SSN: *x*%Er ceramics (inset showing the CIE 1931 *x*-*y* color-matching function; (d) Schematic diagram of UCPL luminescence energy level migration.

Using a 980 nm light source to excite the samples, the Er^{3+} in the ground state $^4I_{15/2}$ energy level absorb the photons (ground state absorption, GSA) and migrate to the excited state $^4I_{11/2}$ energy level [43]. Some of these Er^{3+} can populate the $^4F_{7/2}$ energy level by upconversion of two-step excitation (excited state absorption, ESA). Subsequently multiphonon relaxation occurs, and the Er^{3+}

sequentially relax to the $^2H_{11/2}$, $^4S_{3/2}$, and $^4F_{9/2}$ energy levels, generating emitted light by radiative relaxation to the ground state (Fig. 3d). Due to the small energy difference of the energy levels, a large number of Er^{3+} in the $^4F_{7/2}$ energy level relax to the $^2H_{11/2}$ energy level and then quickly relax further to the $^4S_{3/2}$ energy level. This leads to the formation of weak green light and strong green light (527 nm and 549 nm) from the radiative transitions of the $^2H_{11/2}$ and $^4S_{3/2}$ energy levels to the ground state, respectively. The weak red light corresponds to the transmigration of the $^4F_{9/2}$ energy level to the ground state. Due to the large energy difference, only a small number of Er^{3+} at the $^4S_{3/2}$ energy level will non-radiatively relax to the $^4F_{9/2}$ energy level, resulting in a weak red emission at 667 nm (Fig. 4c). Fig. S3a illustrates that when the Er atom is positioned at the A site, there is a pronounced shift in the position of the neighboring O atom towards the Er atom. This shift leads to the distortion of the NbO_6 octahedron and creates a locally non-uniform chemical bonding environment. In contrast, Fig. S3b shows that the chemical bonding environment in the B-site plane, which is distant from the Er atom, remains highly uniform. This observation indicates that the impact of Er substitution at the A site is relatively localized. Notably, this locally non-uniform chemical bonding environment is known to enhance PL behavior [39].

The functional mechanism of the carrier in 0.825KNN-0.175SSN: *x*%Er ceramic can be explained in reference to impedance spectroscopy. The Zview software is used to fit the impedance data from low frequency to high frequency to understand the resistance contribution of grain boundaries and grains [63]. Based on the equivalent circuit model (Fig. S2a) consisting of a combination of R_{gb}, C_{gb} (grain boundary resistance and capacitance) and R_g, C_g (grain resistance and capacitance) elements, Z' and Z'' (Nyquist or Cole-Cole plots) (Fig. 5a and d) and C' spectra (Fig. 5b and e) were plotted at several temperatures, as well as at 510 °C and Z'' and M'' overlap plots at 510 °C (Fig. 5c and f) to represent the complex impedance behavior of the ceramics. Fig. 5a and d shows that the resistance of grains and grain boundaries decreases with increasing temperature, and a negative temperature coefficient resistance effect (NTCR effect) exists [64]. When $x = 0$, 0.05, a single, regular Debye-like semicircle appears in the Nyquist diagram, indicating that the grain boundary resistance R_{gb} is significantly higher than the grain resistance R_g, and the grain boundary contribution is more closely related to the conductivity behavior. The atomic arrangement near the grain boundary is disordered and electron scattering increases [65]. On the contrary, when $x = 0.10$, 0.15 (Fig. S2b), two semicircular arcs are observed from the figure, where the high-frequency region is related to the grain effect and the low-frequency region is related to the grain boundary effect [66]. This implies that the enhanced resistive contribution of the grains may lead to an increase in the grain size. The distribution of low and high capacitance plateaus in the C' spectrum is related to the grain effect and grain boundary effect [67]. It has been observed that the C' spectrum of 0.825KNN-0.175SSN: 0.05%Er (Fig. 5e) shows a low capacitance plateau (~0.11 nF/cm) in the high-frequency range and a high capacitance plateau (~2.45 nF/cm) in the low-frequency range. In addition, the normalized spectra of Z'' and M'' (Fig. 5c and f) showed that after Er^{3+} modification, the peak positions of Z''/Z''_{max} and M''/M''_{max} had an overlapping tendency, indicating an increase in electrical homogeneity, which improves the resistivity of the 0.825KNN-0.175SSN: 0.05%Er ceramic [68]. The corresponding impedance results are in agreement with the conclusion of fine and uniform grain size distribution exhibited by SEM.

The variation of the thermal conductivity of the grains is shown in Fig. 6a, and the linear variation of $\ln(\sigma T)$ *versus* $1000/T$ proves that there is no phase transition in the temperature range studied. The gradual increase of the conductivity value with temperature proves that the conductivity in this material corresponds to a thermally activated transport process. The linear region of this can be fitted with the Arrhenius equation below:

$$\sigma = \sigma_0 \exp\left(\frac{-E_a}{k_B T}\right) \tag{3}$$

where E_a is the activation energy for grain conductivity, σ is a pre-exponential factor including charge carrier mobility and density of states, k_B is Boltzmann's constant, and T is the Kelvin temperature [66]. When the value of the activation energy (E_a) is less than 1 eV, it is an oxyanionic conduction. On the contrary, an activation energy greater than 1 eV corresponds to electron conduction [69]. Fig. 6a–b shows the Arrhenius fitted line plots and the corresponding E_a values summarized for each component, respectively. As a whole, the E_a value ranges from 0.84 eV to 1.55 eV, which is less than half of the corresponding ceramic E_g (Fig. 4b). Among them, the highest E_a value of 1.55 eV is found at $x = 0.05$. This indicates that this sample has a lower concentration of vacancy defects, which is favorable for transparency. Meanwhile, the $x = 0.10$ and 0.15 samples have smaller E_a values, resulting in lower carrier transport energy barriers. The E_a value of the $x = 0.15$ sample is less than 1 eV, indicating that the conduction process may be mainly caused by the mobility of the oxygen vacancies, with a higher concentration of vacancy defects and lower transparency of the sample. This can be attributed to free electron and vacancy defect generation due to excess Er doping. It can be inferred that the concentration of oxygen vacancies in the system decreases when a small amount of Er^{3+} ions substitute for the A-site, as illustrated by Formula (4):

$$Er_2O_3 + 2V_O^{\cdot\cdot} \xrightarrow{KNN} 2Er_{K/Na}^{\cdot\cdot} + 3O_O^{\times} \tag{4}$$

However, when the Er^{3+} ion is overdoped, the non-equivalent donor substitution will lead to more free electrons to be generated to maintain the electrically neutral state. As shown below:

$$Er_2O_3 \xrightarrow{KNN} 2Er_{K/Na}^{\cdot\cdot} + 3O_O^{\times} + 4e' \tag{5}$$

An additional analysis employing X-ray photoelectron spectroscopy (XPS) was conducted to elucidate the variations in oxygen vacancy defect concentrations within the ceramic samples [70,71]. The obtained spectra, as illustrated in Fig. S4, reveal distinct peaks for the 0.825KNN-0.175SSN and 0.825KNN-0.175SSN: 0.05%Er ceramics, with the O 1s XPS spectra detailed in Fig. 5g–h. The observed three peaks at 529.7, 531.4 eV, and 532.2 eV are respectively attributed to lattice oxygen (O1), oxygen vacancies (O2), and surface-adsorbed oxygen (O3). A quantitative analysis of the relative peak areas of O2, as depicted in Fig. 5i, indicates a reduction in oxygen vacancy concentration from 32.83% to 28.83% in the 0.825KNN-0.175SSN: 0.05%Er ceramic compared to the 0.825KNN-0.175SSN counterpart, consistent with the observed changes in transmittance as shown in Fig. 4a.

The A-site substitution of Er^{3+} may lead to the creation of K/Na vacancies in the 0.825KNN-0.175SSN lattice to balance the excess charge induced by the doping of ions with different valence states. This process may lead to the formation of defective dipoles, whose reorientable properties in the presence of an external electric field play an important role in improving the dielectric properties of 0.825KNN-0.175SSN ceramic [72]. Fig. 7a, b demonstrates the variation of dielectric constant (ε_r) and dielectric loss ($\tan\delta$) with temperature for 0.825KNN-0.175SSN and 0.825KNN-0.175SSN: 0.05%Er ceramic at different frequencies. Compared with 0.825KNN-0.175SSN, 0.825KNN-0.175SSN: 0.05%Er ceramic had a temperature of maximum permittivity (T_m) shifted toward lower

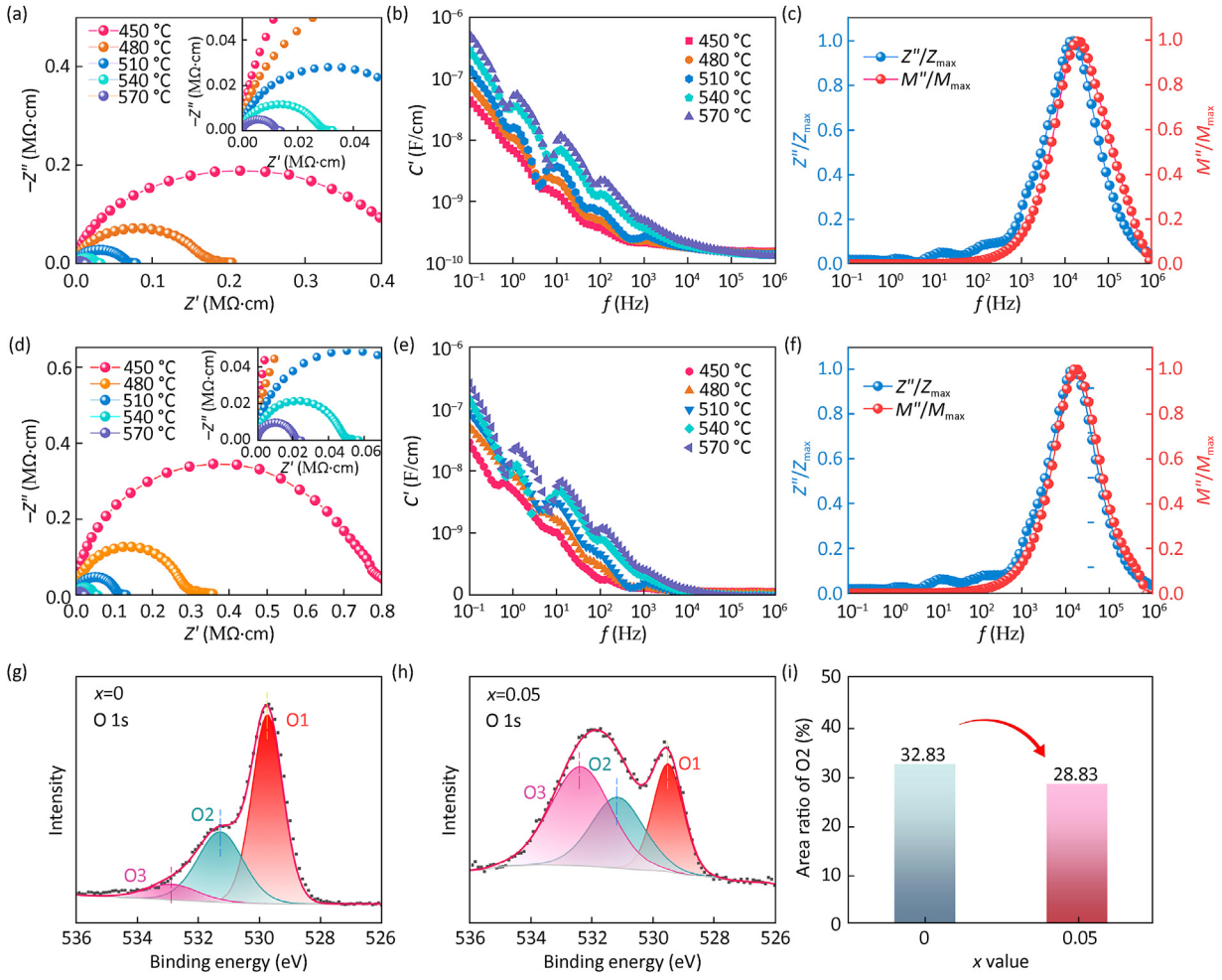

Fig. 5. Composite impedance spectra of (a) 0.825KNN-0.175SSN and (d) 0.825KNN-0.175SSN: 0.05%Er; C' spectra of (b) 0.825KNN-0.175SSN and (e) 0.825KNN-0.175SSN: 0.05%Er; Frequency correlation plots of Z''/Z''_{max} and M''/M''_{max} for (c) 0.825KNN-0.175SSN and (f) 0.825KNN-0.175SSN: 0.05%Er; XPS spectra of O 1s: (g) 0.825KNN-0.175SSN, (h) 0.825KNN-0.175SSN: 0.05%Er, (i) O2 photoelectron peak area change.

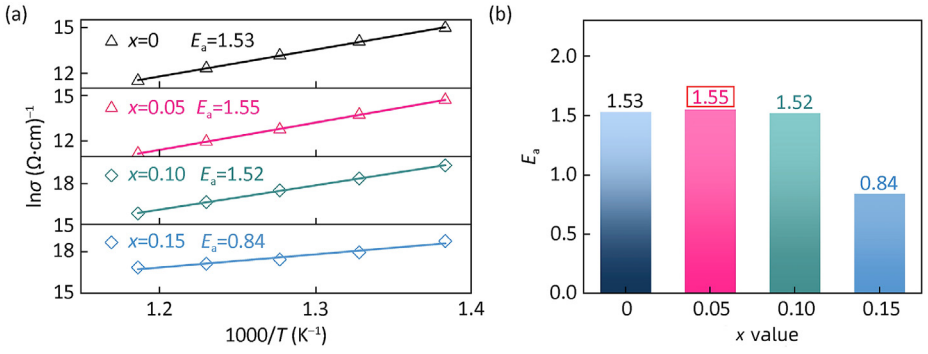

Fig. 6. (a) Arrhenius-type plots of the conductivity with the temperature of 0.825KNN-0.175SSN: x%Er ceramic and (b) the simulated E_a values change diagram.

temperature, and obvious diffusive phase transition and frequency dispersion phenomena appeared, which indicated that the 0.825KNN-0.175SSN: 0.05%Er ceramic exhibited typical relaxation ferroelectric features. This phenomenon may be due to the localized distortion of the 0.825KNN-0.175SSN lattice induced by the doping of Er^{3+} with different radii and valence states, which in turn increases the disorder of the lattice. This distortion disrupts the long-range ferroelectric ordering and favors the generation of polar nanoregions (PNRs). Due to the presence of PNRs and the internal disorder of the ceramic samples, some hysteresis relaxation occurs in the polarization response of the ceramics upon application of an external electric field. The dielectric constant of the material was fitted using the modified Curie-Excise law to further analyze the relaxation behavior of the material. The formula is calculated as follows:

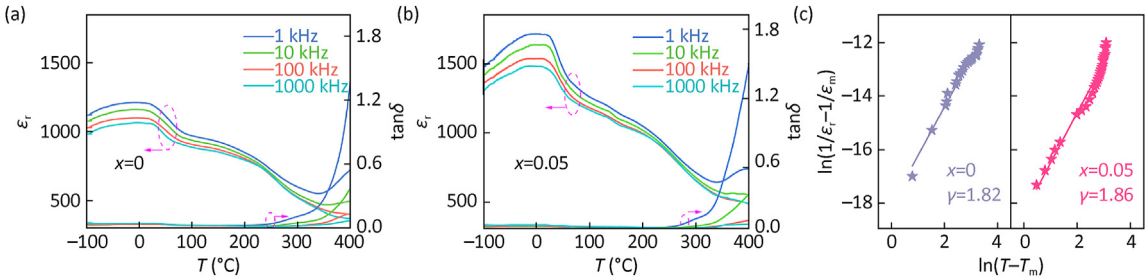

Fig. 7. (a) Temperature-dependent dielectric response of 0.825KNN-0.175SSN and (b) 0.825KNN-0.175SSN: 0.05%Er; (c) $\ln(1/\varepsilon-1/\varepsilon_m)$ as a function of $\ln(T-T_m)$ and the corresponding γ value for 0.825KNN-0.175SSN and 0.825KNN-0.175SSN: 0.05%Er samples, at 1000 kHz.

$$\gamma = \ln(T - T_m)\ln(1/\varepsilon - 1/\varepsilon_m) \quad (6)$$

where γ is the diffusion coefficient, T_m is the temperature corresponding to the maximum dielectric constant, and ε_m is the maximum dielectric constant. The change in the value of γ from 1 to 2 marks the transition from a normal ferroelectric to an ideal relaxing ferroelectric [66]. Fig. 7c shows the $\ln(1/\varepsilon-1/\varepsilon_m)$ at 1000 kHz *versus* $\ln(T-T_m)$, the diffusivity γ reaches 1.86 when $x = 0.05$, which indicates that the 0.825KNN-0.175KNN: 0.05%Er sample exhibits more significant relaxation characteristics.

The *P*–*E* rings of 0.825KNN-0.175SSN: *x*%Er ceramic samples and the corresponding evolution of maximum polarization (P_{max}) and residual polarization strength (P_r) measured at room temperature at 100 kV/cm are shown in Fig. 8a and c. The *P*–*E* rings of 0.825KNN-0.175SSN: *x*%Er ceramic are shown in Fig. 8a. The tilted elongated *P*–*E* rings indicate that the ceramics exhibit relaxation ferroelectric behavior, which is promising for energy storage capacitor applications. Both P_{max} and P_r first decrease and then increase with increasing Er content, which is attributed to the fact that a moderate amount of Er_2O_3 disrupts the long-range ferroelectric ordering of the 0.825KNN-0.175SSN ceramics, which leads to the creation of polarized nanoregions (PNRs) and enhances the relaxation properties of the ceramics. The energy storage density and energy storage efficiency can be expressed by the following equations [73]:

$$W_{rec} = \int_{P_r}^{P_{max}} E dP \quad (7)$$

where W_{rec}, W_{loss}, P_{max}, P_r, and E represent the recoverable energy density, energy loss, maximum polarization strength, residual polarization strength, and electric field of the sample, respectively. By calculating the *P*–*E* curves, the energy storage characteristics of 0.825KNN-0.175SSN: *x*%Er ceramics under the action of 100 kV/cm electric field are shown in Fig. 8b, and P_{max} reaches a maximum value of 29.55 μC/cm^2 at $x = 0.05$ and 86% efficiency. The *P*–*E* ring of 0.825KNN-0.175SSN ceramics becomes thinner after moderate Er doping, which indicates that Er doping can improve its energy storage performance. To further explore the energy storage properties of 0.825KNN-0.175SSN: 0.05%Er ceramics, the unipolar *P*–*E* rings were measured under different applied electric fields, as shown in Fig. 8d. The *P*–*E* ring consistently maintained a low P_r value over the applied electric field range (Fig. 8f). As a result, the η remained at a relatively high level as the P_{max} value increased linearly. Finally, an energy density of 2.03 J/cm^3 was obtained at

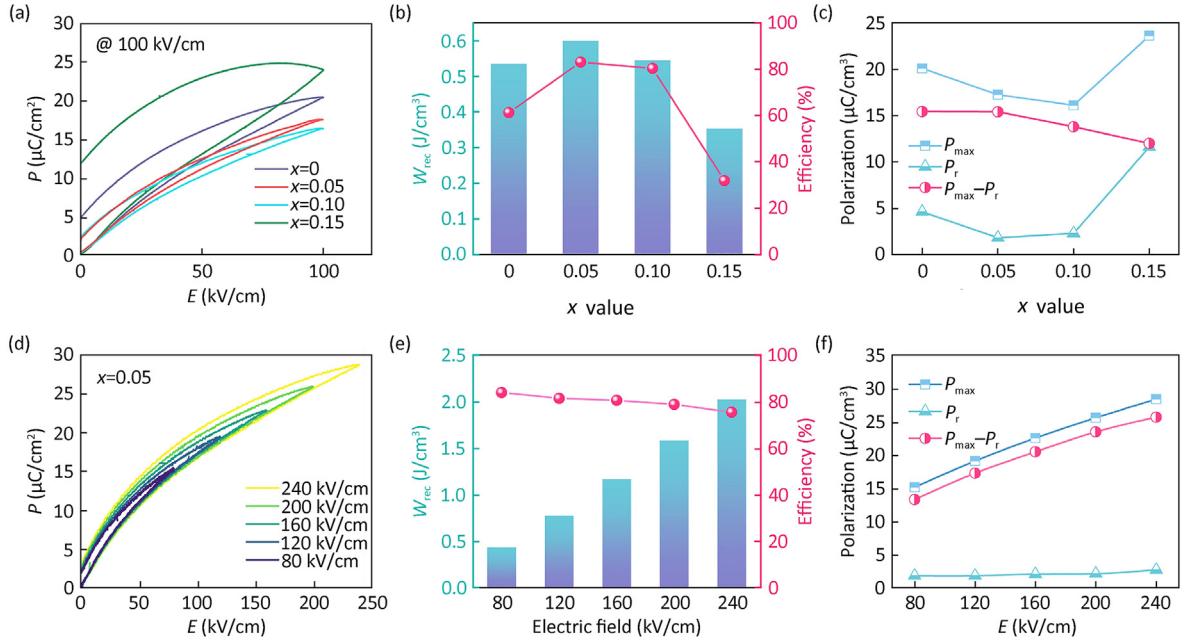

Fig. 8. (a) Unipolar *P*–*E* hysteresis loop, (b) W_{rec} and η values and (c) P_{max}, P_r, and P_{max}–P_r values for 0.825KNN-0.175SSN: *x*%Er ceramic at 100 kV/cm; (d) Unipolar *P*–*E* hysteresis loops; (e) W_{rec} and η values; (f) P_{max}, P_r, and P_{max}–P_r values for 0.825KNN-0.175SSN: 0.05%Er ceramics at different electric fields.

Table 1
Comparison of 0.825KNN-0.175SSN: 0.05%Er ceramic with ceramics of different systems, including KNN-based and BNT-based ceramics, in terms of recoverable energy storage density, energy storage efficiency, and light transmission rate.

Material	W_{rec} (J/cm^3)	η (%)	T (%)	Ref.
$NaNbO_3$-0.04$CaZrO_3$	0.55	63.00		[67]
KNN-0.015 EB	1.85	69.00	<50.0	[74]
BNT-0.5NN	5.14	79.65	32.0	[75]
0.9KNN-0.1ST: 0.1Er	0.86	<60.00	39.1	[76]
KNN-0.08BaMN	0.80		>60.0	[77]
0.9BNT-0.1BZT: 0.6%Er^{3+}	2.95	51.30	28.0	[78]
0.825KNN-0.175SSN:0.05%Er	2.03	75.67	48.0	This work

240 kV/cm while η reached 75.67% (Fig. 8e). Table 1 compares the performance of 0.825KNN-0.175SSN: 0.05%Er ceramics with previously reported ceramics of different systems including KNN-based and BNT-based ceramics [67,74–78], in terms of recoverable energy storage density, energy storage efficiency, and light transmission. The results show that the 0.825KNN-0.175SSN: 0.05% Er ceramics are competitive in terms of electrical and optical performance.

For further clarification for the underlying mechanism of the crystal structure transformation of Er_2O_3 incorporated in the 0.825KNN-0.175SSN system, crystal orbitals overlapping totals (COOP) simulations have been performed. The integrated COOP value (ICOOP) provides a way to quantify the bonding strength [79]. COOP is the bonding information extracted from the density states obtained by weighting the overlap totals and is used to show the strength and nature of the positive bonding (COOP >0) or anti-bonding (COOP <0) interactions, where a COOP value of zero indicates the absence of bonding interactions. The COOP curves of the Nb–O interactions before and after doping are presented in Fig. 9a–b, showing that there are significant Nb–O bonding interactions within the valence band, with two significant bonding peaks between −20 eV and 0 eV attributed to hybridization interactions between the 4d orbitals of the Nb atoms in the B-site and the O-2p orbitals. The O_p and O_a refer to the planar oxygen atoms and the apical of the oxygen atom. Compared to 0.825KNN-0.175SSN, the 0.825KNN-0.175SSN: 0.05%Er structure has a slightly lower bond energy for Nb–O_p and an increased bond energy for Nb–O_{a1}, which may lead to distortions of the O_p planes and their neighboring NbO_6 octahedra. This is in agreement with the result of improved crystal structure symmetry with displacement of B-site ions along the [001] direction exhibited in Fig. 2e.

The stability of ferroelectricity in perovskite materials has been reported to be closely related to the degree of hybridization between the outermost d orbitals of the B-site atoms and the p orbitals of the oxygen atoms [28,80,81]. In KNN materials,

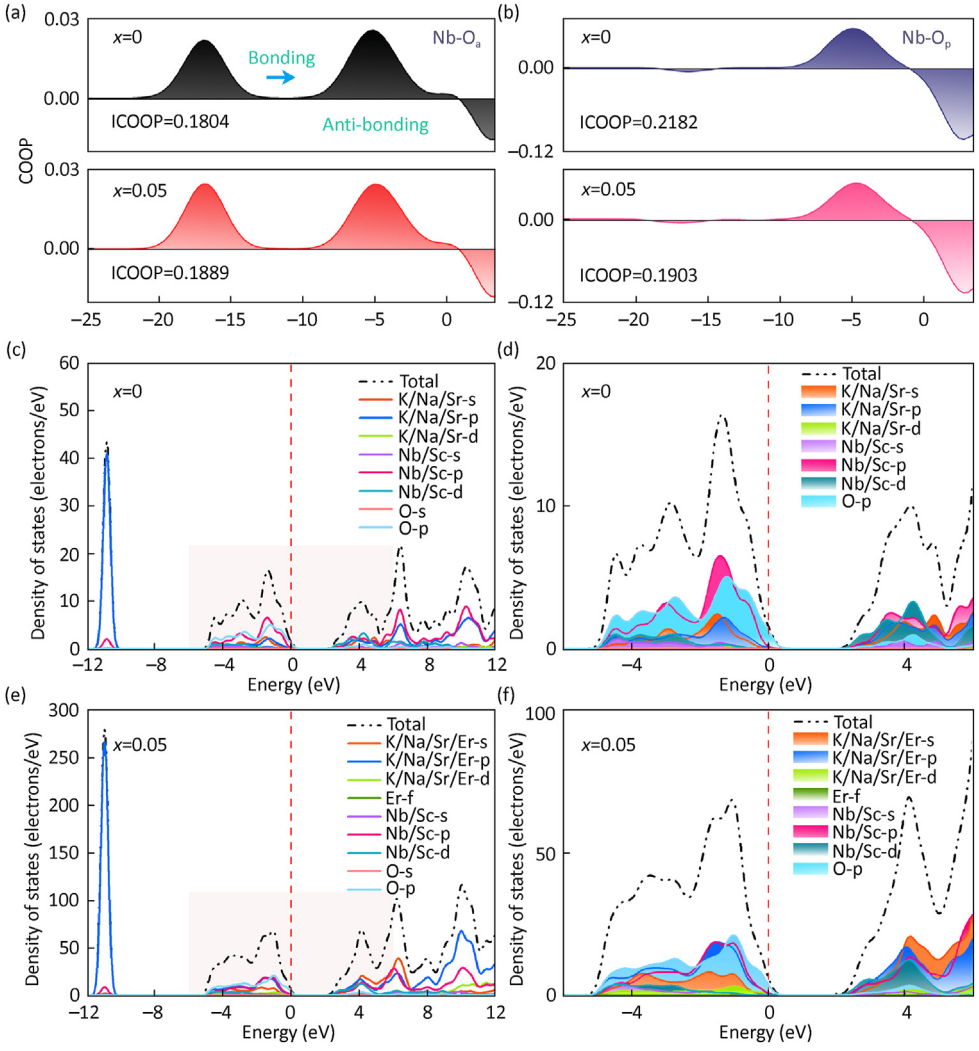

Fig. 9. Interaction COOP of (a) Nb–O_a and (b) Nb–O_p for the 0.825KNN-0.175SSN and 0.825KNN-0.175SSN: *x*%Er structures; (c–f) Total and partial density of states plots.

ferroelectricity mainly originates from the strong hybridization between the Nb-4d orbitals and the O-2p orbitals [60,76]. The hybridization effect between the 4d orbitals of the B-site Nb atoms and the 2p orbitals of the O atoms significantly attenuates the intrinsic short-range repulsive force, thus enhancing the stability of the ferroelectric structure. The quantification of this degree of hybridization can effectively assess the strength of ferroelectricity [76]. To deeply explore the mechanism of the change in ferroelectricity of the KNN-SSN system by Er_2O_3 doping, electronic density of states calculations were carried out. Fig. 9c–f demonstrates the total density of states (TDOS) and partial density of states (PDOS) analyses for the 0.825KNN-0.175SSN structure and the 0.825KNN-0.175SSN: 0.05%Er structure. As shown in Fig. 9c and e, the PDOS values of K/Na/Sr ions at the A-site in the KNN-SSN system are lower than 4 eV, indicating weak hybridization with the O-2p orbital. The valence band (−6 to 0 eV range) consists mainly of the synergistic contribution of the O-2p orbitals with the other ion orbitals, while the conduction band (2–6 eV range) is mainly dominated by the Nb-4d state, with a small contribution from O-2p. This suggests that the transfer of electrons from the valence band to the conduction band involves hybridization between the Nb-4d state and the O-2p state. In the doped KNN-SSN: Er system, the DOS distributions near the top of the valence band (VBM) and the bottom of the conduction band (CBM) are extended to higher energy ranges, and the difference in the PDOS values between the A-site ions and the O-2p state decreases, and the hybridization effect is enhanced. Meanwhile, the hybridization between the B-site Nb-4d orbitals and the O-2p orbitals is weakened, and the long-range ordered ferroelectric states are disrupted, which may lead to the coupled relaxation behavior that occurs in the 0.825KNN-0.175SSN: 0.05%Er ceramic. This is consistent with the low P_r phenomenon in the unipolar P–E loops of Fig. 8d.

4. Conclusions

Supported by first-principles calculations, the feasibility of simultaneously enhancing energy storage and transparent luminescence properties is investigated by doping various concentrations of Er^{3+} into ferroelectric KNN ceramic system. The ceramic samples of $(K_{0.5}Na_{0.5})NbO_3$-0.175$Sr(Sc_{0.5}Nb_{0.5})O_3$: x%Er were synthesized using the conventional solid-state reaction method. The results demonstrate that local lattice distortion and effective grain refinement enable the 0.825−0.175SSN: 0.05%Er ceramic to exhibit excellent energy storage properties, with a W_{rec} of 2.03 J/cm^3 and an η-value of 75.67% under an electric field of 240 kV/cm for $x = 0.05$. In the meanwhile, the low concentration of vacancy defects and a high band gap ($E_g = 3.105$ eV) result in a transmittance of 53% for light of 1100 nm, and strong green upconversion luminescence. The high resistance (0.103 MΩ at 510 °C) and the electrical homogeneity of the samples strongly support their superior energy storage performance. The density-of-states map of Nb−O bonding, along with the analysis of ICOOP value variations, elucidates the mechanism underlying the relaxor ferroelectricity of the system. The presence of localized, inhomogeneous bonding environments on the A-site planes suggests that the A-site substitution of Er has a localized effect, which enhances the photoluminescence performance and lower remnant polarization with energy storage efficiency of the system. This study provides a robust theoretical and experimental foundation for developing rare-earth ion-doped lead-free ferroelectric ceramic with novel and multiple optoelectronic functions.

CRediT authorship contribution statement

Zhichao Gong: Writing – original draft, Formal analysis, Data curation. **Haojie Yue:** Methodology. **Kailing Fang:** Writing – review & editing, Software. **Kun Guo:** Writing – review & editing, Supervision, Investigation. **Kang Li:** Investigation, Data curation. **Chong Guo:** Software, Resources. **Huacheng Zhang:** Data curation. **Ziliang Deng:** Formal analysis. **Zhiyong Liu:** Writing – review & editing, Resources. **Bing Xie:** Writing – review & editing, Investigation. **Pu Mao:** Writing – review & editing, Methodology. **Jinshan Lu:** Validation, Resources. **Shifeng Guo:** Resources, Investigation, Conceptualization. **Kui Yao:** Writing – review & editing. **Francis Eng Hock Tay:** Writing – review & editing, Software.

Declaration of competing interest

The authors declare that they have no known competing financial interests or personal relationships that could have appeared to influence the work reported in this paper.

Acknowledgments

This project is partially supported by the National Natural Science Foundation of China (Grant No. 52002164, No. 52060020, No. 52162018, No. 52162019) and the Natural Science Foundation of Jiangxi Province of China (Grant No. 20242BAB25224). The author from Institute of Materials Research and Engineering acknowledges supports from A*STAR, under RIE2020 AME Programmatic Fund (Grant No. A20G9b0135). This study was partially supported by the High Performance Computing Service of the Modern Educational Technology and Information Center of Nanchang Hangkong University.

Appendix A. Supplementary data

Supplementary data to this article can be found online at https://doi.org/10.1016/j.jmat.2024.100993.

References

[1] Kyerematen NA, Brousse T, Pech D. Microsupercapacitors as miniaturized energy-storage components for on-chip electronics. Nat Nanotechnol 2016;12(1):7–15.
[2] Zhang P, Xue S, Wang J. New challenges of miniaturization of electronic devices: Electromigration and thermomigration in lead-free solder joints. Mater Des 2020;192:108726.
[3] Dinis H, Mendes PM. A comprehensive review of powering methods used in state-of-the-art miniaturized implantable electronic devices. Biosens Bioelectron 2021;172:112781.
[4] Liu H, Zhang G, Zheng X, Chen F, Duan H. Emerging miniaturized energy storage devices for microsystem applications: from design to integration. Int J Extrem Manuf 2020;2(4):042001.
[5] Zhang P, Wang F, Yu M, Zhuang X, Feng X. Two-dimensional materials for miniaturized energy storage devices: from individual devices to smart integrated systems. Chem Soc Rev 2018;47(19):7426–51.
[6] Tricoli A, Nasiri N, De S. Wearable and miniaturized sensor Technologies for Personalized and Preventive Medicine. Adv Funct Mater 2017;27(15):1605271.
[7] Huang Y, Zhu M, Huang Y, Pei Z, Li H, Wang Z, et al. Multifunctional energy storage and conversion devices. Adv Mater 2016;28(38):8344–64.
[8] Huang Z, Shao G, Li L. Micro/nano functional devices fabricated by additive manufacturing. Prog Mater Sci 2023;131:101020.
[9] Guo Y, Wei X, Gao S, Yue W, Li Y, Shen G. Recent Advances in Carbon material-based multifunctional sensors and their applications in electronic Skin systems. Adv Funct Mater 2021;31(40):2104288.
[10] Lee JH, Cho K, Kim JK. Age of Flexible electronics: Emerging Trends in Soft multifunctional sensors. Adv Mater 2024;36(16):2310505.
[11] Yao K, Chen S, Lai SC, Yousry YM. Enabling distributed Intelligence with ferroelectric Multifunctionalities. Adv Sci 2021;9(1):2103842.

[12] Wu S, Fu B, Zhang J, Du H, Zong Q, Wang J, et al. Superb energy storage capability for $NaNbO_3$-based ceramics featuring labyrinthine submicro-domains with clustered lattice distortions. Small 2023;19(45):2303915.
[13] Wang H, Wu S, Fu B, Zhang J, Du H, Zong Q, et al. Hierarchically polar structures induced superb energy storage properties for relaxor $Bi_{0.5}Na_{0.5}TiO_3$-based ceramics. Chem Eng J 2023;471:144446.
[14] Qiao X, Sheng A, Wu D, Zhang F, Chen B, Liang P, et al. A novel multifunctional ceramic with photoluminescence and outstanding energy storage properties. Chem Eng J 2021;408:127368.
[15] Zhao C, Huang Y, Wu J. Multifunctional barium titanate ceramics via chemical modification tuning phase structure. InfoMat 2020;2(6):1163–90.
[16] Bai Y, Tofel P, Palosaari J, Jantunen H, Juuti J. A Game changer: a multifunctional perovskite exhibiting giant ferroelectricity and narrow bandgap with potential application in a truly monolithic multienergy harvester or sensor. Adv Mater 2017;29(29):1700767.
[17] Zhang Q, Luo L, Gong J, Du P, Li W, Yuan G. Photoluminescence, thermoluminescence and reversible photoluminescence modulation of multifunctional optical materials Pr^{3+} doped $K_xNa_{1-x}NbO_3$ ferroelectric ceramics. J Eur Ceram Soc 2020;40(12):3946–55.
[18] Cheng S, Zhang K, Li C, Zhang B, Chen J, Sun K, et al. Improved piezoelectric and luminescent properties in Sm-modified $Bi_{0.5}Na_{0.5}TiO_3BaTiO_3$ multifunctional ceramics. J Materiomics 2024;10(4):803–10.
[19] Wang Y, Chen Y, Zheng D. Development of multifunctional electronic-ceramics with piezoelectric effect and varistor behavior. Ceram Int 2022;48(18):26818–27.
[20] Huang Y, Zhao C, Zhong S, Wu J. Highly tunable multifunctional $BaTiO_3$-based ferroelectrics *via* site selective doping strategy. Acta Mater 2021;209:116792.
[21] Yue H, Fang K, Chen T, Jing Q, Guo K, Liu Z, et al. First-principle study on correlate structural, electronic and optical properties of Ce-doped $BaTiO_3$. Crystals 2023;13(2):255.
[22] Zheng B, Fan J, Chen B, Qin X, Wang J, Wang F, et al. Rare-earth doping in Nanostructured inorganic materials. Chem Rev 2022;122(6):5519–603.
[23] Kumar V, Ntwaeaborwa OM, Soga T, Dutta V, Swart HC. Rare earth doped Zinc Oxide Nanophosphor powder: a Future material for solid state lighting and solar Cells. ACS Photonics 2017;4(11):2613–37.
[24] Sun L-D, Wang Y-F, Yan C-H. Paradigms and challenges for Bioapplication of rare earth upconversion luminescent Nanoparticles: small size and tunable emission/excitation spectra. Acc Chem Res 2014;47(4):1001–9.
[25] Lei P, Feng J, Zhang H. Emerging biomaterials: Taking full advantage of the intrinsic properties of rare earth elements. Nano Today 2020;35:100952.
[26] Zhou S, Lin D, Su Y, Zhang L, Liu W. Enhanced dielectric, ferroelectric, and optical properties in rare earth elements doped PMN-PT thin films. J Adv Ceram 2020;10(1):98–107.
[27] Ren P, Yang J, Liu Y, Wang X, Zhang H, Jia Y, et al. Modulation of photoluminescence properties by poling and quenching strategy in rare earth ions doped $Na_{1/2}Bi_{1/2}TiO_3$-based ceramics. Chem Eng J 2024;490:151577.
[28] Xia L, Liu X, Mao Z, Cai Y, Zhu J, Xie J, et al. Temperature/electric field induced photoluminescence-modulation effect in dysprosium-doped barium titanate ferroelectric ceramics. J Materiomics 2024;10(5):1117–25.
[29] Khatua DK, Agarwal A, Kumar N, Ranjan R. Probing local structure of the morphotropic phase boundary composition of $Na_{0.5}Bi_{0.5}TiO_3$–$BaTiO_3$ using rare-earth photoluminescence as a technique. Acta Mater 2018;145:429–36.
[30] Granados del Águila A, Do TTH, Xing J, Jee WJ, Khurgin JB, Xiong Q. Efficient up-conversion photoluminescence in all-inorganic lead halide perovskite nanocrystals. Nano Res 2020;13(7):1962–9.
[31] Ye Z, Lin X, Wang N, Zhou J, Zhu M, Qin H, et al. Phonon-assisted up-conversion photoluminescence of quantum dots. Nat Commun 2021;12(1):4283.
[32] Ren X, Jin L, Peng Z, Chen B, Qiao X, Wu D, et al. Regulation of energy density and efficiency in transparent ceramics by grain refinement. Chem Eng J 2020;390:124566.
[33] Liu Q, Pan E, Deng H, Liu F, Li J-F. Dy^{3+}doped (K,Na)NbO_3-based multifunctional ceramics for achieving enhanced temperature-stable piezoelectricity and non-contact optical temperature sensing performance. Inorg Chem Front 2023;10(8):2359–69.
[34] Li W, Hao J, Li W, Du J, Fu P, Sun W, et al. Electrical properties and luminescence properties of $0.96(K_{0.48}Na_{0.52})(Nb_{0.95}Sb_{0.05})$–$0.04Bi_{0.5}(Na_{0.82}K_{0.18})_{0.5}ZrO_3$-*x*Sm lead-free ceramics. J Adv Ceram 2020;9(1):72–82.
[35] Jia Q, Zhang Q, Sun H, Hao X. High transmittance and optical storage behaviors in Tb^{3+} doped $K_{0.5}Na_{0.5}NbO_3$-based ferroelectric materials. J Eur Ceram Soc 2021;41(2):1211–20.
[36] Chen Q, Gao T, Lang R, Tan Z, Xing J, Zhu J. Achieving outstanding temperature stability in KNN-based lead-free ceramics for energy storage behavior. J Eur Ceram Soc 2023;43(6):2442–51.
[37] Sun Z, Zhao S, Wang T, Jing H, Guo Q, Gao R, et al. Achieving high overall energy storage performance of KNN-based transparent ceramics by ingenious multiscale designing. J Mater Chem A 2024;12(27):16735–47.
[38] Lin J, Ge G, Zhu K, Bai H, Sa B, Yan F, et al. Simultaneously achieving high performance of energy storage and transparency *via* A-site non-stoichiometric defect engineering in KNN-based ceramics. Chem Eng J 2022;444:136538.
[39] Wu L, Tan Z, Zheng T, Wu J. KNN–Eu transparent ferroelectrics: local structure and luminescent property. J Am Ceram Soc 2023;106(11):6664–74.
[40] Lin J, Zhou Y, Lu Q, Wu X, Lin C, Lin T, et al. Reversible modulation of photoenergy in Sm-doped $(K_{0.5}Na_{0.5})NbO_3$ transparent ceramics via photochromic behavior. J Mater Chem A 2019;7(33):19374–84.
[41] Lin J, Lu Q, Xu J, Wu X, Lin C, Lin T, et al. Outstanding optical temperature sensitivity and dual-mode temperature-dependent photoluminescence in Ho^{3+}-doped (K,Na)NbO_3–$SrTiO_3$ transparent ceramics. J Am Ceram Soc 2019;102(8):4710–20.
[42] Golesorkhi B, Nozary H, Fürstenberg A, Piguet C. Erbium complexes as pioneers for implementing linear light-upconversion in molecules. Mater Horiz 2020;7(5):1279–96.
[43] Wu X, Lin J, Xu Z, Zhao C, Lin C, Wang H, et al. Defect Management and multimode optoelectronic Manipulations *via* Photo-Thermochromism in smart Windows. Laser Photon Rev 2021;15(10):2100211.
[44] Lin J, Zhai J, Wu X, Shen B, Ye H, Wang H. Simultaneously improved transparency, photochromic contrast and Curie temperatureviarare-earth ion modification in KNN-based ceramics. Inorg Chem Front 2021;8(8):2027–35.
[45] Wang Y, Fullon R, Acerce M, Petoukhoff CE, Yang J, Chen C, et al. Solution-processed MoS_2/Organolead Trihalide perovskite Photodetectors. Adv Mater 2017;29(4):1603995.
[46] Atkinson CM, Alpay SP, Guziewski M. First-principles analysis of the local atomic environment in calcium lanthanum sulfide ceramics. Acta Mater 2024;271:119881.
[47] Chai Q, Zhang F, Zhou Q, Peng Z, Wu D, Liang P, et al. Superior energy storage properties and optical transparency in $K_{0.5}Na_{0.5}NbO_3$-based dielectric ceramics via multiple synergistic Strategies. Small 2023;19(19):2207464.
[48] Rahman A, Park S, Min Y, Hwang G-T, Choi J-J, Hahn B-D, et al. An easy approach to obtain large piezoelectric constant in high-quality transparent ceramics by normal sintering process in modified potassium sodium niobate ceramics. J Eur Ceram Soc 2020;40(8):2989–95.
[49] Fu J, Zuo R. Structural evidence for the polymorphic phase boundary in (Na,K)NbO_3 based perovskites close to the rhombohedral-tetragonal phase coexistence zone. Acta Mater 2020;195:571–8.
[50] Huan Y, Wei T, Wang Z, Lei C, Chen F, Wang X. Polarization switching and rotation in KNN-based lead-free piezoelectric ceramics near the polymorphic phase boundary. J Eur Ceram Soc 2019;39(4):1002–10.
[51] Yang W, Han Z, Zheng G. The influences of lattice distortion on the antiferroelectric transition and relaxation of oxygen vacancies in high-entropy perovskites $(Bi_{0.2}Na_{0.2}Ba_{0.2}K_{0.2}X_{0.2})TiO_3$ with X=Ca, Sr or La. Scripta Mater 2021;203:114096.
[52] Yang S, Zuo C, Du F, Chen L, Jie W, Wei X. Submicron $Sr_{0.7}Bi_{0.2}TiO_3$ dielectric ceramics for energy storage via a two-step method aided by cold sintering process. Mater Des 2023;225:111447.
[53] Wu YJ, Huang YH, Wang N, Li J, Fu MS, Chen XM. Effects of phase constitution and microstructure on energy storage properties of barium strontium titanate ceramics. J Eur Ceram Soc 2017;37(5):2099–104.
[54] Zhang Y, Gao G, Deng Y, Liu Y, He Y, Song J, et al. Coupling donor doping and anion vacancy in Ni_3Se_4 battery-type cathode for large-capacity and high-rate charge storage. Energy Storage Mater 2024;67:103284.
[55] Zhu Y, Li X, Guo Z, Sun H, Zhang Q, Hao X. Optical temperature sensing and luminescent switching properties in Pr/Er-doped $(K_{0.5}Na_{0.5})NbO_3$ materials. J Am Ceram Soc 2020;103(5):3205–16.
[56] Huan Y, Wang X, Fang J, Li L. Grain size effect on piezoelectric and ferroelectric properties of $BaTiO_3$ ceramics. J Eur Ceram Soc 2014;34(5):1445–8.
[57] Gao Y, Zhu X, Yang B, Shi P, Kang R, Yuan Y, et al. Grain size modulated $(Na_{0.5}Bi_{0.5})_{0.65}Sr_{0.35}TiO_3$-based ceramics with enhanced energy storage properties. Chem Eng J 2022;433:133584.
[58] Xiao Z, Yu S, Li Y, Ruan S, Kong LB, Huang Q, et al. Materials development and potential applications of transparent ceramics: a review. Mater Sci Eng R Rep 2020;139:100518.
[59] Milisavljevic I, Zhang M, Jiang Q, Liu Q, Wu Y. Transparent Electro-Optic Ceramics: processing, materials, and applications. J Materiomics 2025;11(2):100872.
[60] Lin J, Wang Y, Xiong R, Sa B, Shi C, Zhai J, et al. Tailoring micro-structure of eco-friendly temperature-insensitive transparent ceramics achieving superior piezoelectricity. Acta Mater 2022;235:118061.
[61] Liu Z, Fan H, Zhao Y, Dong G, Jo W. Optical and tunable dielectric properties of $K_{0.5}Na_{0.5}NbO_3$–$SrTiO_3$ ceramics. J Am Ceram Soc 2015;99(1):146–51.
[62] Hříbalová S, Pabst W. Transmittance predictions for transparent alumina ceramics based on the complete grain size distribution or a single mean grain size replacing the whole distribution. J Eur Ceram Soc 2022;42(12):5093–107.
[63] Bongiorno V, Michailidou E, Curioni M. Towards the automated interpretation of impedance spectra from organic coatings using neural networks. Corrosion Sci 2024;230:111922.
[64] Mohanty NK, Satpathy SK, Behera B, Nayak P, Choudhary RNP. Complex impedance properties of $LiSr_2Nb_5O_{15}$ ceramic. J Adv Ceram 2012;1(3):221–6.
[65] Mu S, Samolyuk GD, Wimmer S, Troparevsky MC, Khan SN, Mankovsky S, et al. Uncovering electron scattering mechanisms in NiFeCoCrMn derived concentrated solid solution and high entropy alloys. npj Comput Mater 2019;5(1):1.
[66] Zheng Q, Xie B, Tian Y, Wang Q, Luo H, Liu Z, et al. High recoverable energy density of $Na_{0.5}Bi_{0.5}TiO_3$-based ceramics by multi-scale insulation regulation and relaxor optimization strategy. J Materiomics 2024;10(4):845–56.
[67] Liu Z, Lu J, Mao Y, Ren P, Fan H. Energy storage properties of $NaNbO_3$-$CaZrO_3$ ceramics with coexistence of ferroelectric and antiferroelectric phases. J Eur Ceram Soc 2018;38(15):4939–45.
[68] Su Q, Ma Z, Zhu J, Sun N, Zhao Y, Lu C, et al. Excellent energy-storage performance in BNT-SST-LMN lead-free relaxor ferroelectric ceramics with high

electrical homogeneity. ACS Appl Energy Mater 2022;5(12):15247–56.
[69] Voronkova VI, Leonidov IA, Kharitonova EP, Belov DA, Patrakeev MV, Leonidova ON, et al. Oxygen ion and electron conductivity in fluorite-like molybdates $Nd_5Mo_3O_{16}$ and $Pr_5Mo_3O_{16}$. J Alloys Compd 2014;615:395–400.
[70] Jia X, Zhang J, Wang L, Wang J, Du H, Yao Y, et al. Role of oxygen-vacancy in piezoelectric properties and fatigue behavior of $(Bi_{0.5}Na_{0.5})_{0.93}Ba_{0.07}Ti_{1+x}O_3$ ceramics. J Am Ceram Soc 2019;102(9):5203–12.
[71] Wu L, Zhang J, Du H, Chen J, Yu H, Liu Y, et al. Chemical nature of the enhanced energy storage in A-site defect engineered $Bi_{0.5}Na_{0.5}TiO_3$-based relaxor ferroelectrics. J Alloys Compd 2022;905:164183.
[72] Tian S, Wang B, Li B, Guo Y, Zhang S, Dai Y. Defect dipole stretching enables ultrahigh electrostrain. Sci Adv 2024;10(28):eadn2829.
[73] Dai Z, Li D, Zhou Z, Zhou S, Liu W, Liu J, et al. A strategy for high performance of energy storage and transparency in KNN-based ferroelectric ceramics. Chem Eng J 2022;427:131959.
[74] Xing J, Huang Y, Wu B, Liu H, Tan Z, Chen Q, et al. Energy storage behavior in $ErBiO_3$-doped (K,Na)NbO_3 lead-free piezoelectric ceramics. ACS Appl Electron Mater 2020;2(11):3717–27.
[75] Luo W, Wu M, Han Y, Zhou X, Liu L, He Q, et al. Enhanced optical transmittance and energy-storage performance in $NaNbO_3$-modified $Bi_{0.5}Na_{0.5}TiO_3$ ceramics. J Am Ceram Soc 2023;106(8):4723–31.
[76] Gao L, Liu Z, Ren P, Liang R, Li T, Guo K, et al. Inhibiting oxygen vacancies and twisting NbO_6 octahedron in erbium modified KNN-based multifunctional ceramics. J Materiomics 2024;10(1):179–89.
[77] Chao X, Ren X, Zhang X, Peng Z, Wang J, Liang P, et al. Excellent optical transparency of potassium-sodium niobate-based lead-free relaxor ceramics induced by fine grains. J Eur Ceram Soc 2019;39(13):3684–92.
[78] Yang J, Guan P, Zhang Y, Zhu X, Wang H, Yang C, et al. High energy storage density achieved in BNT-based ferroelectric translucent ceramics under low electric fields. J Am Ceram Soc 2024;107(9):6294–306.
[79] Yue H, Fang K, Gong Z, Chen L, Guo K, Liu H, et al. The mechanism of ferroelectric phase transformation in Gd_2O_3 modified BCZT ceramics: experimental studies and first-principles calculations. Ceram Int 2024;50(7):10416–26.
[80] Ruiz FM, Anthoniappen J, Tu C-S, Chen P-Y, Chen C-S, Wang S-F, et al. Role of O 2*p*-Ti 3*d* orbital hybridization in dielectric and ferroelectric properties of barium zirconate titanate ceramics. Mater Res Bull 2020;129:110905.
[81] Zhang N, Lv X, Zhang X-X, Lyu J, Yang S-W, Wu J. Low-temperature dielectric relaxation associated with NbO_6 octahedron distortion in antimony modified potassium sodium niobate ceramics. J Mater Sci Technol 2022;115:189–98.

Zhichao Gong is a master's student at the College of Power and Energy, Nanchang Hangkong University. His current research interests primarily focus on multifunctional ferroelectric materials and first-principles theoretical calculations.

Kun Guo received her Ph.D. degree in Mechanical Engineering from National University of Singapore. She is now working in Nanchang Hangkong University as an associate professor. Her current research interests include piezoelectric materials for sensors, actuators, transducers, and energy storage devices, energy harvester design and preparation, machine learning and first-principles study related to dielectric materials.